



HAL
open science

Evolution of Cu-In Catalyst Nanoparticles under Hydrogen Plasma Treatment and Silicon Nanowire Growth Conditions

Weixi Wang, Éric Ngo, Pavel Bulkin, Zhengyu Zhang, Martin Foldyna, Pere Roca I Cabarrocas, Erik V Johnson, Jean-Luc Maurice

► **To cite this version:**

Weixi Wang, Éric Ngo, Pavel Bulkin, Zhengyu Zhang, Martin Foldyna, et al.. Evolution of Cu-In Catalyst Nanoparticles under Hydrogen Plasma Treatment and Silicon Nanowire Growth Conditions. *Nanomaterials*, 2023, 13 (14), pp.2061. 10.3390/nano13142061 . hal-04298103v2

HAL Id: hal-04298103

<https://hal.science/hal-04298103v2>

Submitted on 24 Nov 2023

HAL is a multi-disciplinary open access archive for the deposit and dissemination of scientific research documents, whether they are published or not. The documents may come from teaching and research institutions in France or abroad, or from public or private research centers.

L'archive ouverte pluridisciplinaire **HAL**, est destinée au dépôt et à la diffusion de documents scientifiques de niveau recherche, publiés ou non, émanant des établissements d'enseignement et de recherche français ou étrangers, des laboratoires publics ou privés.

1 **Evolution of Cu-In catalyst nanoparticles under hydrogen plasma treatment and silicon**
2 **nanowire growth conditions**

3 Weixi Wang¹, Eric Ngo¹, Pavel Bulkin¹, Zhengyu Zhang², Martin Foldyna¹, Pere Roca i Cabarrocas¹,
4 Erik V. Johnson¹, and Jean-Luc Maurice^{1*}

5 ¹ Laboratoire de physique des interfaces et couches minces, École polytechnique, CNRS, IPParis,
6 91120 Palaiseau, France

7 ² Université Paris-Saclay, CNRS, Ecole Normale Supérieure Paris-Saclay, CentraleSupélec,
8 Laboratoire LuMIn, 91190 Gif-sur-Yvette, France

9 E-mail: jean-luc.maurice@polytechnique.edu

10 **Abstract**

11 We report silicon nanowire (SiNW) growth with a novel Cu-In bimetallic catalyst using a plasma-
12 enhanced chemical vapor deposition (PECVD) method. We study the structure of the catalyst
13 nanoparticles (NPs) throughout a two-step process that includes a hydrogen plasma pre-treatment at
14 200 °C and the SiNW growth itself in a hydrogen-silane plasma at 420 °C. We show that the H₂-
15 plasma induces a coalescence of the Cu-rich cores of as-deposited thermally evaporated NPs, that does
16 not occur when the same annealing is applied without plasma. The SiNW growth process at 420 °C
17 induces a phase transformation of the catalyst cores to Cu₇In₃; while a hydrogen plasma treatment at
18 420 °C without silane can lead to the formation of the Cu₁₁In₉ phase. *In-situ* transmission electron
19 microscopy experiments show that the SiNWs synthesis with Cu-In bimetallic catalyst NPs follows an
20 essentially vapor-solid-solid process. By adjusting the catalyst composition, we manage to obtain
21 small-diameter SiNWs – below 10 nm, among which we observe the metastable hexagonal diamond
22 phase of Si, which is predicted to have a direct bandgap.

23 **Key words:** Cu-In nanoparticle, plasma treatment, silicon nanowire, PECVD, TEM

24 **1. Introduction**

25

26 Semiconductor nanowires (NWs) are attracting an increasing attention because of their
27 application prospects in electronic, sensing, optoelectronic and photovoltaic devices [1-7]. The most
28 common methods for preparing these nano-objects are based on the vapor-liquid-solid (VLS) and
29 vapor-solid-solid (VSS) growth processes, where a NW precipitates from a catalyst particle where its
30 constituting elements are maintained in supersaturation [8]. The electrical and optical properties of the
31 NWs are strongly size- and structure-dependent [9-12], and catalyst NPs play a vital role in
32 determining the NW size, structure, morphology, distribution, and orientation. In this respect, using
33 compound catalysts gives an additional degree of freedom to monitor these parameters: *for example,*
34 *Ga-Au {Lugstein, 2007 #315} and Cu-Au {Maksimova, 2018 #316} catalysts have been proven*
35 *advantageous in adjusting SiNW geometrical shape, size and orientation; Bi-Sn {Yu, 2015 #317}*
36 *catalyst can lead to a doping effect in SiNWs; Al-Au {Behroudj, 2019 #318} catalyst yields reliable*
37 *epitaxial growth of SiNWs on single-crystalline silicon substrates; Ag-Au {Chou, 2012 #319} catalyst*
38 *are employed to form compositionally abrupt interfaces of Si/Ge/Si heterojunctions in NWs.* In our
39 previous works on the mechanisms of growth of SiNWs [13, 15], we have illustrated how the use of a
40 mixed catalyst – where one of the components is liquid and the other one is solid – increases even
41 more these possibilities, in a mode we have called liquid-assisted-VSS (LAVSS). Since then, the
42 tuning of the shape or the orientation of the nanowires by LAVSS has also been used in the growth of
43 compound semiconductor NWs [14]. The system we have explored in the refs. [13, 15] was that of
44 Cu-Sn, which resulted in catalysts made of solid Cu_3Si and liquid Sn during growth. With this type of
45 catalyst, we were able to prepare SiNWs with the metastable hexagonal 2H structure [15] that is
46 predicted to have a direct bandgap [16]. Indium, which has a similar phase diagram with Cu [17],
47 possesses an even lower melting point than Sn (157 °C vs. 232 °C) and appealed to us as the next
48 candidate to be associated with Cu. If, as a member of column 3 in the periodic table, it is a p-type
49 dopant for Si, its solubility in Si is very low [18], so that its benefit as a catalyst overpasses, at least at
50 this stage of our study, the drawback of a possible unwanted doping. Let us mention, by the way, that
51 the control of its introduction into the Si lattice during growth, through a carefully designed catalyst
52 composition, would allow one an additional control of the NW properties [19].

53

54 Copper-indium alloys have been studied a lot, as they are used in catalysis, thin film solar
55 cells manufacturing, and interconnections in the electronics industry, [20-26]. The reactions of Cu-In
56 alloys as catalysts for electrochemical reduction of CO₂ [27-29], as precursors for the growth of
57 CuInSe₂ solar cells [30-32], and as solders for the fabrication of Cu/In/Cu joints for the silicon
58 interconnections components [33-35], have been widely studied. Recently, it is reported that Cu-In
59 bimetallic NPs have been successfully used as catalyst for the growth of SiNWs by a plasma-enhanced
60 CVD (PECVD) method [36]. Therefore, a detailed characterization of the Cu-In catalyst NPs is
61 required for a better understanding of their influence on the SiNW growth mechanism. In addition,
62 since the impact of plasma on the catalyst NPs [37] brings an additional complexity to the reactions
63 between Cu and In for the synthesis of SiNWs at relatively low temperature, exploring the structure of
64 the Cu-In NPs under various plasma conditions during NW growth is of great importance for a better
65 control of SiNW fabrication. In this work, we study SiNW growth by using a bimetallic catalyst of Cu-
66 In. To understand the growth mechanism, we observe the catalyst structure evolution by *ex-situ* TEM
67 throughout the SiNW growth process in a PECVD reactor; we also use *in-situ* TEM to visualize the
68 critical stage of plasma ignition and analyze the catalyst structure during SiNW growth. We
69 demonstrate the phenomenon of crystallization and phase transformation in Cu-In NPs induced by
70 hydrogen and hydrogen-silane plasmas. On the other hand, Cu-In alloys are widely used nano-solder
71 materials as they can form small-diameter NPs [35, 38], which is promising to obtain small-diameter
72 SiNWs with the metastable 2H hexagonal diamond phase [15, 39]. We report in this study the
73 discovery of the 2H phase in the SiNWs synthesized with the Cu-In catalyst.

74 **2. Materials and Methods**

75 The bimetallic Cu-In NPs are prepared in a BOC Edwards Auto 306 Evaporator FL 400. Cu is
76 first evaporated on the substrates; then, the Cu-loaded crucible is changed for an In-loaded one and In
77 is evaporated on top of Cu. The nominal thickness of each of the evaporated elements is thus measured

78 independently by a quartz microbalance in the thermal evaporator. The sensitivity of the quartz
79 microbalance, together with the speed at which the experimentalist moves the shutter when the desired
80 value is displayed, lead to a limited precision in the deposited matter that may significantly vary from
81 one deposit to the next. Based on energy dispersive X-ray spectroscopy performed on deposits made
82 on carbon-coated gold TEM grids, we evaluate this error to +/- 20% on the final atomic proportions.
83 Given the wetting of the metals on the substrates, NPs naturally form by atom aggregation upon
84 thermal evaporation. Each run includes at least two types of substrates: cleaved Si (001) samples, for
85 NW growth, and carbon-coated gold TEM grids for the characterization of the NPs by TEM. Specific
86 runs include in addition a Protochips™ SiC heating membrane for the *in-situ* TEM experiments.

87 The substrates undergoing the standard *ex-situ* treatment are then loaded into a PECVD
88 reactor operating at a radio frequency (RF) of 13.56 MHz for the fabrication of SiNWs. A two-step
89 NW growth process is applied on the as-deposited Cu-In NPs after the vacuum reaches 5×10^{-5} mbar
90 in the PECVD chamber. A schematic diagram of a SiNW growth experiment in a PECVD reactor is
91 shown in Supplementary Information (SI), Figure S4.

92 - Step I – hydrogen plasma pre-treatment at 200 °C. For this step, the H₂ flow rate, the gas
93 pressure P , the RF plasma power density and the duration time t are 100 sccm, 0.8 mbar, 56.7 mW/cm²
94 and 2 min, respectively. To evaluate the effect of plasma, we compare the Cu-In NPs after the plasma
95 treatment with the NPs having experienced the same temperature anneal but without plasma. To follow
96 the effect of plasma in real time, we make the same experiment *in-situ*, in the TEM (with smaller
97 catalysts deposited on the Protochips™ heating membranes);

98 - Step II – SiNW growth at 420 °C. For this step, a second plasma treatment is carried out in
99 the same run in the PECVD reactor by adding a SiH₄ flow of 5 sccm to 100 sccm H₂ and changing the
100 process parameters to the following values: P of 1.42 mbar, RF power density of 17 mW/cm² for $t = 3$
101 min. To understand respectively the effect of the plasma and that of adding silane, we compare the Cu-
102 In catalyst NPs at the head of the obtained SiNWs with *i*) those NPs that have undergone exactly the

103 same plasma pre-treatment at 200 °C as mentioned above and the 420°C anneal treatment but the latter
 104 in vacuum, and ii) the NPs that have undergone the 420°C plasma treatment, but with only hydrogen
 105 and no SiH₄ in the plasma (the other experimental parameters remain unchanged as in step I).

106 Table 1 lists the detailed parameters of six groups of experiments of plasma treatment and
 107 SiNW growth in this study. Group 1 to 5 are carried out in a PECVD reactor named Plasfil, using a
 108 bimetallic catalyst with a nominal thickness of 1 nm In/1 nm Cu on carbon-coated gold grid substrates
 109 for the convenience of TEM characterization. Group 6 is an *in situ* TEM experiment using 0.6 nm In/0.2
 110 nm Cu as catalyst on a SiC TEM heating membrane. And group 7 to 10 are also performed in Plasfil
 111 PECVD reactor, using the same experimental condition as in group 3, but on (001) c-Si substrates.

112 Table 1. Detailed PECVD parameters of the plasma treatment and the SiNW growth

Group	Catalyst and substrate	Step I: hydrogen plasma treatment				Step II: SiNW growth			
		<i>T</i> (°C)	H ₂ flow rate (sccm)	<i>P</i> (mbar)	Power density (mW/cm ₂)	<i>T</i> (°C)	H ₂ + SiH ₄ flow rate (sccm)	<i>P</i> (mbar)	Power density (mW/cm ₂)
1	1 nm In/1 nm Cu, carbon-coated gold TEM grid	200	100	0.8	56.7				
2		200	100	0.8	0				
3		200	100	0.8	56.7	420	100 + 5	1.42	17
4		200	100	0.8	56.7	420	0	1.42	0
5		420	100	0.8	56.7				
6	0.6 nm In/0.2 nm Cu, SiC membrane	250	30		50 W	370	30 + 1.5	3×10 ⁻²	50 W
7	1 nm In/1 nm Cu	Growth parameters are the same as group 3, but on (001) c-Si substrates							
8	0.1 nm In/0.1 nm Cu								
9	0.1 nm In								
10	0.05 nm In/0.05 nm Cu								

113

114 The structures of the Cu-In NPs before and after the plasma treatment are characterized in two
 115 TEM microscopes for high resolution imaging and selected area diffraction patterns (SADP): a Jeol
 116 2010F and a Thermo Fisher Titan 80-300 named “Nan’eau”. The acceleration voltages utilized are 200
 117 kV for the Jeol 2010F TEM, and 300 kV for the Titan TEM, respectively. The diffraction patterns are

118 interpreted with the help of the JEMS software [40, 41] and CIF files from the Inorganic Crystal
119 Structure Database – ICSD. After growth, SiNWs are observed by scanning electron microscopy
120 (SEM) using a Hitachi S-4800. Some SiNWs are transferred from the c-Si substrates to carbon-coated
121 gold TEM grids for Energy Dispersive X-ray spectroscopy (EDX) analysis in TEM Nan’eau.

122 The *in-situ* TEM study of the Cu-In catalysts is carried out in an environmental TEM (ETEM)
123 named “NanoMAX”: it is a modified Thermo Fisher Titan 80-300 equipped with an aberration
124 corrector, which allows a high resolution of 0.08 nm in TEM mode; it is also equipped with a Gatan
125 UltraScan 1000 camera which can record *in situ* videos at a rate of four 1k×1k frames per second.
126 Heating is performed using the SiC heating membranes of the Fusion sample holder from
127 Protochips™. Each heating chip is delivered with a digital abacus giving the temperature as a function
128 of the applied power. We measured an error of +/- 5 °C, on the melting points of pure Sn and pure In
129 large particles (theoretical points at 157 °C and 232 °C, respectively). In most of the chips, no
130 temperature variations could be detected over the utilized part ($\sim 50\text{-}\mu\text{m}$)² of the heated area. The
131 NanoMAX TEM is equipped with an Aura-Wave electron cyclotron resonance (ECR) plasma source
132 from SAIREM, which is situated at about 0.4 m from the sample. We use a plasma power of 50 W.
133 The recombination of ions and electrons takes place very fast, so that no ion gets to the sample [42,
134 43]. However, the recombination of H atoms to make H₂ molecules is much less efficient, so that the
135 presence of H neutral atoms remains significant at the sample level [43]. In the *in-situ* experiments
136 Steps I and II are replaced by respectively a Step I’ where the substrate is heated up to 250°C and the
137 H₂ flow, injected into the plasma chamber connected to the TEM column, set to 30 sccm, and a Step
138 II’, where the substrate temperature is set to 370 °C and the SiH₄ flow to 1.5 sccm; the latter gas is
139 injected directly into the microscope (not through the plasma chamber). The pressure in the column is
140 3×10^{-2} mbar during growth.

141

142 **3. Results and discussion**

143 3.1. Evolution of bimetallic Cu-In catalyst NPs throughout the process

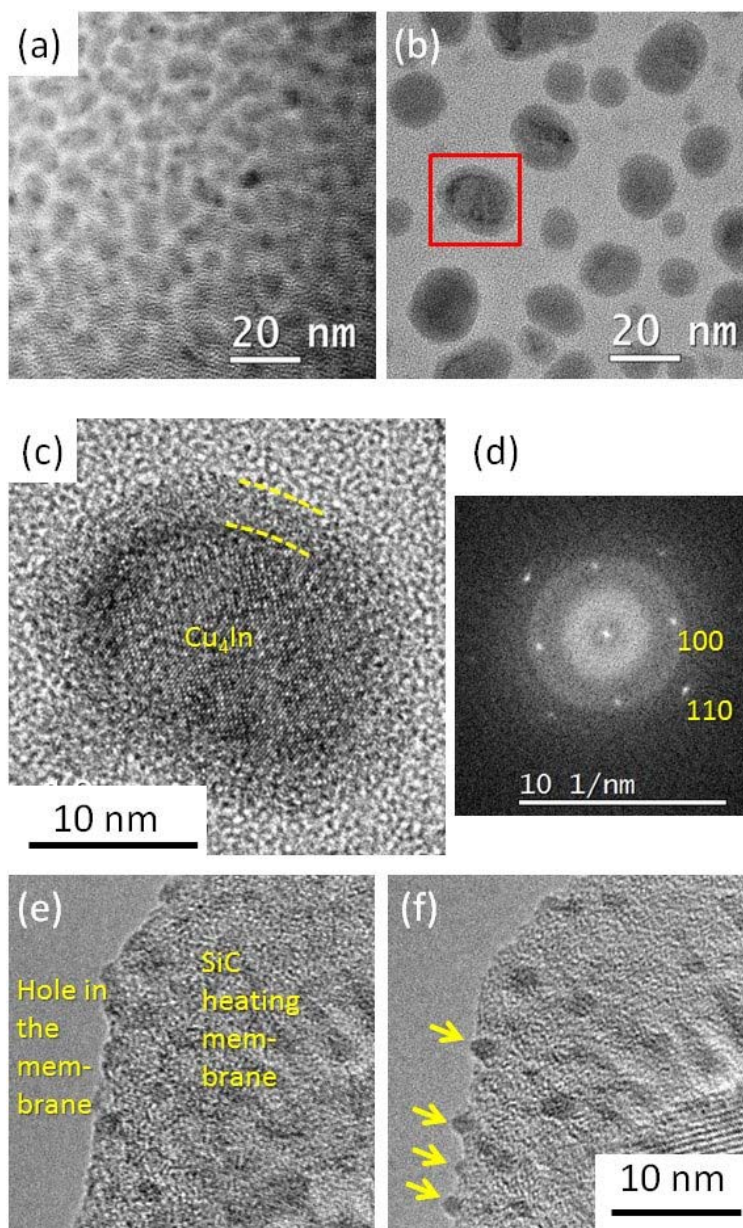
144 We observe the structure of Cu-In NPs in the as-deposited state and throughout the SiNW
145 growth process. The standard In/Cu thickness we use is 1/1 nm (nominally 69.6 at.% Cu), unless
146 otherwise mentioned. Given the uncertainties mentioned in the experimental section, the actual Cu
147 percentage may vary, especially between deposits made with a several-month interval by different
148 experimentalists, between ~40 % and ~90 %. The as-deposited NPs are mostly amorphous, with
149 diameters ranging from 4 to 10 nm, as shown in Figure 1a.

150 3.1.1. 200 °C H₂ plasma treatment

151 We firstly perform the hydrogen plasma pre-treatment at 200 °C for 2 minutes in the PECVD
152 reactor on the as-deposited NPs (see Table 1, Group 1). The bimetallic catalyst NPs adopt a core-shell
153 structure: a crystalline core is covered by an amorphous shell (Figure 1b, c). The diameters of the
154 catalyst NPs after such a hydrogen plasma treatment range from 4 to 24 nm, as shown in the histogram
155 of NP diameter distribution in Figure 4d. A SADP on a larger area exhibits diffraction rings that are
156 best fitted by the high-temperature phase Cu₄In-β (see SI, Figure S2d, ICSD file #109480)
157 [44], normally stable above 574-576 °C [45-47]. The high-resolution image of a NP in the [001] zone
158 axis exhibits the typical square pattern of the bcc structure of this phase (Figure 1c, d). Let us note,
159 however, that the β-phase thus defined remains close to the α-phase (solid solution in fcc Cu), where
160 ordering of In atoms would bring a new line at 0.3 nm. . Annealing the as-deposited Cu-In NPs at
161 200 °C for 2 minutes (see Table 1, group 2) without plasma does not result in such a drastic
162 reorganization nor crystallization: the NPs undergo some coalescence but keep a worm-like shape (see
163 SI, Figure S1b). Thus, indium would stay amorphous upon deposit and plasma treatment, while copper
164 would crystallize in quasi-spherical shapes during annealing, incorporating some of the In, only if
165 exposed to the plasma; In would keep sticking to Cu in all cases.

166 The goal of the *in-situ* experiment in NanoMAX (see Table 1, group 6) is to image the
167 dewetting and coalescence of the NPs. The deposit used in this case concerns smaller amounts of In
168 and Cu: (resp. 0.6 nm and 0.2 nm; nominally 42 at.% Cu), with the aim of forming smaller catalysts

169 with a larger liquid part, better suited for obtaining the 2H-phase in the Si NWs made with them [15].
170 It is performed at 250°C and 3×10^{-2} mbar H₂. As-deposited NPs are hardly visible in the TEM (Figure
171 1d); switching ON the plasma triggers their dewetting indeed, almost instantaneously, and drastically
172 increases their TEM contrast (Figure 1e) (see also Supplementary Material, Movie1). We associate this
173 effect with a fast reduction of the In surface oxide, together with a change in the surface energy
174 balance, due to coverage by adsorbed H atoms. Perhaps due to a lesser amount of matter, and to a
175 surface quite different from that of amorphous carbon, we observe very little coalescence with such
176 small particles.



177

178 Figure 1. (a-c) TEM images of the bimetallic catalyst NPs obtained with a nominal thickness
 179 of 1 nm In/1 nm Cu: (a) as-deposited catalyst NPs; (b) NPs after a hydrogen plasma pre-treatment at
 180 200 °C for 2 minutes (group 1); and (c) enlargement of the red-squared area in (b); (d) the power
 181 spectrum of the fast Fourier transform (FFT) of (c), exhibiting the pattern of the [001] zone axis of
 182 Cu_4In . (e, f) Catalyst NPs obtained on a SiC TEM heating membrane with a nominal thickness of 0.6
 183 nm In/0.2 nm Cu before and after exposing them at 250 °C to a hydrogen plasma *in situ* in the TEM

184 (group 6); the yellow arrows in (e) show the plasma-dewetted Cu-In NPs.

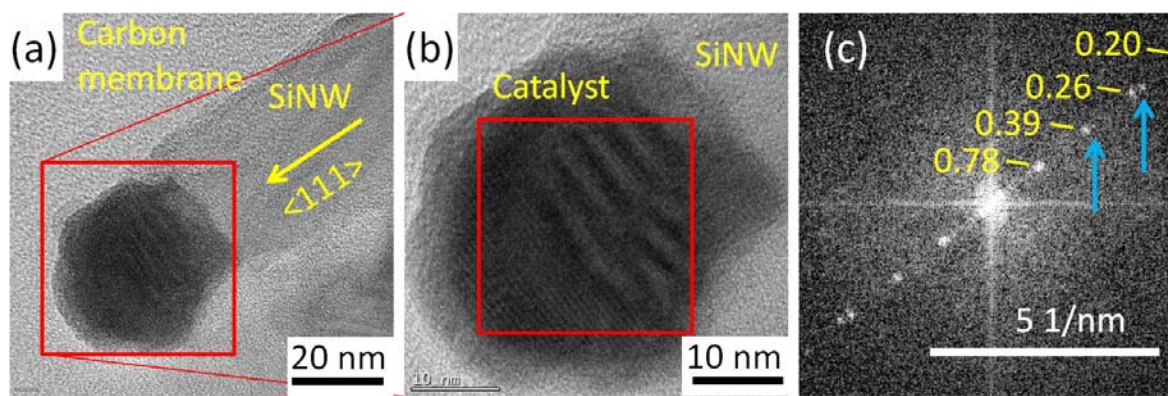
185 3.1.2. 420 °C plasma treatment and Si nanowire growth

186 After the hydrogen plasma pre-treatment at 200 °C, we carry out SiNW growth at 420 °C by
187 exposing the Cu-In NPs to a hydrogen-silane plasma for 3 minutes and analyze the structure of the Cu-
188 In NPs after the initial stage of SiNW growth (see Table 1, group 3). SiNWs with Cu-In catalyst NPs
189 on top are obtained after this process. Figure 2a,b shows a high-resolution TEM (HRTEM) image of a
190 catalyst NP of 1 nm In/1 nm Cu after the synthesis of SiNW. The FFT image of the catalyst (Figure 2c)
191 indicates spots corresponding to 0.78, 0.39, 0.26 and 0.20 nm interplanar distances, which represent a
192 ~2% dilatation compared to interplanar spacings of (-110), (-220), (-330) and (-440) planes of Cu_7In_3
193 (δ) [48]. In addition, we note, close to the interface with the SiNW, the presence of shorter spacings,
194 making moirés when superimposed with the former in Figure 2a,b, and generating additional spots in
195 the FFT (blue arrows in Figure 2c). These spacings would belong to the (002) (0.37 nm) and (003)
196 (0.24 nm) planes of Cu_3Si - η . We thus have a clue of the presence of Cu_3Si , which is usually found in
197 the catalysts that contain copper during the growth of SiNWs [13, 15, 49]. Moreover, no solid
198 evidence of other intermetallic phases of Cu and In or their oxides have been found in the FFT
199 patterns. We performed EDX analysis on a catalyst NP after SiNW growth to verify its composition
200 (see SI, Figure S3). The detected atomic percentage of Cu/(Cu+In) is about 72%, which is close to the
201 nominal Cu at.% value (69.6%) in the 1 nm In/1 nm Cu deposit used, and is also close to the nominal
202 Cu at.% value (70%) in the Cu_7In_3 (δ) phase.

203 In order to try and better understand the role of plasma, we have set a control group in step II
204 in order to verify that the formation of Cu_7In_3 (δ) phase only results from the hydrogen-silane plasma
205 treatment rather than the elevated temperature (see Table 1, group 4). The TEM results, displayed in
206 the SI (Figure S2), show that the catalyst NPs that have been annealed at 420 °C for the same time
207 duration, but in vacuum, without being processed by plasma, keep the same crystalline structure of
208 Cu_4In as those obtained from step I. Weaker rings in Figure S2e could be due to other Cu-In

209 intermetallic phases, but the majority of the diffracted intensity undoubtedly comes for the Cu_4In formed
210 earlier.

211

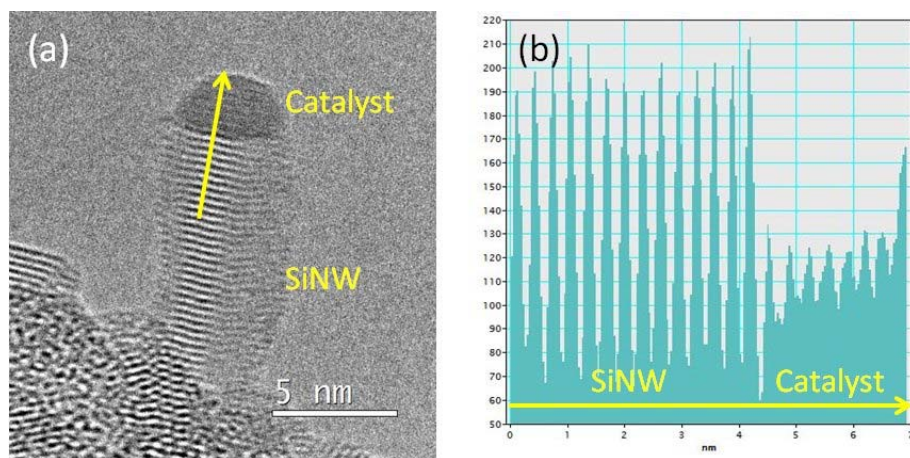


212

213 Figure 2. (a) HRTEM image of a Cu-In catalyst NP at a SiNW tip, obtained after SiNW
214 growth at 420 °C for 3 minutes (group 3); (b) enlargement of the catalyst area in (a); (c) power
215 spectrum of the FFT of the red-squared area in (b): the numbers indicate the lattice spacings (in nm)
216 corresponding to the main spots, belonging to $\text{Cu}_7\text{In}_{3-\delta}$; the blue arrows indicate secondary spots
217 generated by the presence of Cu_3Si .

218 However, as we know that catalysts undergo major changes during cooling of the specimen
219 [13], we tried and observed the growth of SiNWs *in-situ*, in the NanoMAX microscope (see Table 1,
220 group 6). We kept for this the 0.6-nm In/0.2-nm Cu deposit shown in Figure 1e-f. Observing growth in
221 an exact zone axis was not possible, but a SiNW was oriented so that the Si (111) planes perpendicular
222 to the growth direction were visible (Figure 3). The crystalline contrast in the catalyst demonstrates
223 that at least a part of the NP is crystalline. In other frames (see Supplementary Material, Movie2),
224 roundish shapes and absence of contrast indicate that the catalyst may also have a liquid character.
225 Therefore, as in the case of Cu-Sn [13, 15], we could have a liquid-assisted vapor-solid-solid (LAVSS)
226 growth mechanism. Quite strangely, the interplanar distance visible in the catalyst in Figure 3b varies
227 continuously, from 0.38 nm close to the interface with the SiNW, to 0.27 nm at the top. It is thus
228 difficult to conclude on the phase(s) present; let us note that the 0.38 value sits in between the 0.37 and

229 0.39 nm measured after *ex situ* growth (see above).

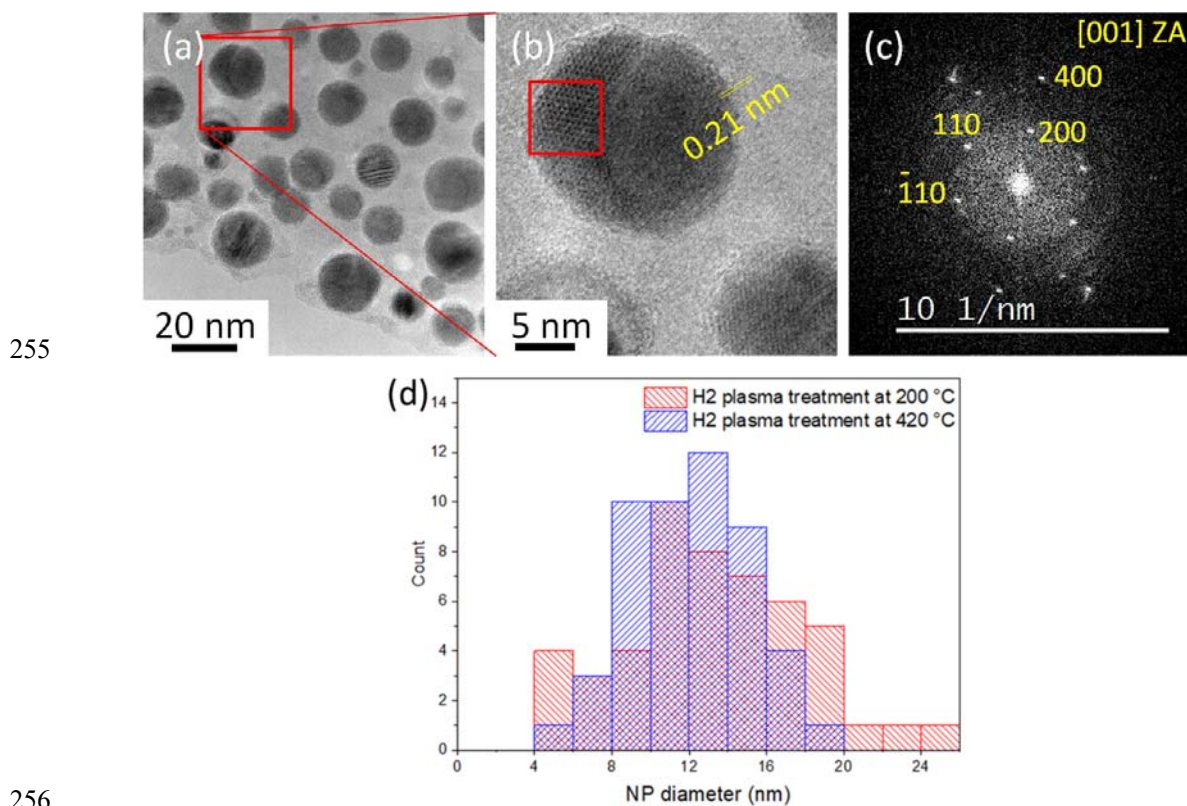


230

231 **Figure 3.** (a) SiNW growing *in situ* (group 6) in the NanoMAX TEM (frame from Movie2 in
232 the Supplementary Material), with a catalyst from the In-0.6 nm/Cu-0.2 nm deposit shown in Figure
233 1e; (b), intensity profile exhibiting the presence of reticular contrast in the catalyst, demonstrating that
234 at least a part of it is crystalline.

235 It is mentioned above that the Cu_7In_3 (δ) phase has been obtained after SiNW growth with a
236 hydrogen-silane plasma at 420 °C. In order to verify which gas plays a major role in this plasma-
237 induced phase transformation phenomenon, we processed the as-deposited Cu-In NPs only in
238 hydrogen plasma at 420 °C for 2 minutes in the PECVD reactor, applying NW growth conditions but
239 without SiH_4 (see Table 1, group 5), in such a way as to isolate the effects of the SiH_4 on the catalyst
240 microstructure (Figure 4). The Cu-In NPs obtained after a hydrogen plasma treatment at 420 °C have
241 diameters mostly ranging from 4 to 20 nm. (Figure 4a and d). We have obtained the $\text{Cu}_{11}\text{In}_9$ structure
242 [50] (see SI, Figure S2f, and ICSD file #238715) which is both different from the Cu_4In found at
243 200 °C (Figure S2d) and from the Cu_7In_3 found when silane is introduced in the plasma at 420°C
244 (Figure 2). Figure 4b shows a HRTEM image of a phase-separated Cu-In NP and Figure 4c displays
245 the FFT of its left-hand part (red-squared area in Figure 4b). The FFT pattern is that of the [001] zone
246 axis of $\text{Cu}_{11}\text{In}_9$, with spots of the (200), (-110) and (110) atomic planes of $\text{Cu}_{11}\text{In}_9$ (respective
247 interplanar distances of 0.52 nm and 0.40 nm). The crystalline phase on the right part of the NP shows

248 atomic planes with an interplanar distance of 0.21 nm, which can belong to the (110) planes of Cu₄In
 249 or the (111) planes of Cu. Thus, switching to the SiNW growth conditions, but without SiH₄, promotes
 250 the development of the metallic Cu₁₁In₉ phase in the nanoparticles, with a possible switch of the
 251 remaining original phase from Cu₄In to α-Cu. Quite interestingly, we thus observe a relative decrease
 252 of Cu content in the compound, compared to the SiH₄ case (Cu₁₁In₉ vs. Cu₇In₃), while the missing
 253 copper stays in the NPs under the form of Cu:In-α or Cu₄In-β, in the present case, and under the form
 254 of Cu₃Si in the silane case (Figure 2).



257 **Figure 4.** TEM of Cu-In NPs obtained after H₂-plasma treatment at 420 °C for 2 min (group
 258 5). (a) General view; (b) HRTEM image of the red square in (a), detailing a Cu-In NP with two
 259 separated phases; (c) FFT image of the red-squared area in (b), which we index in terms of the Cu₁₁In₉
 260 [001] zone axis; and (d) histogram of diameter distributions of Cu-In catalyst NPs after hydrogen
 261 plasma treatment at 200 °C (group 1) and at 420 °C (group 5).

262 3.1.3. Catalyst evolution: summary

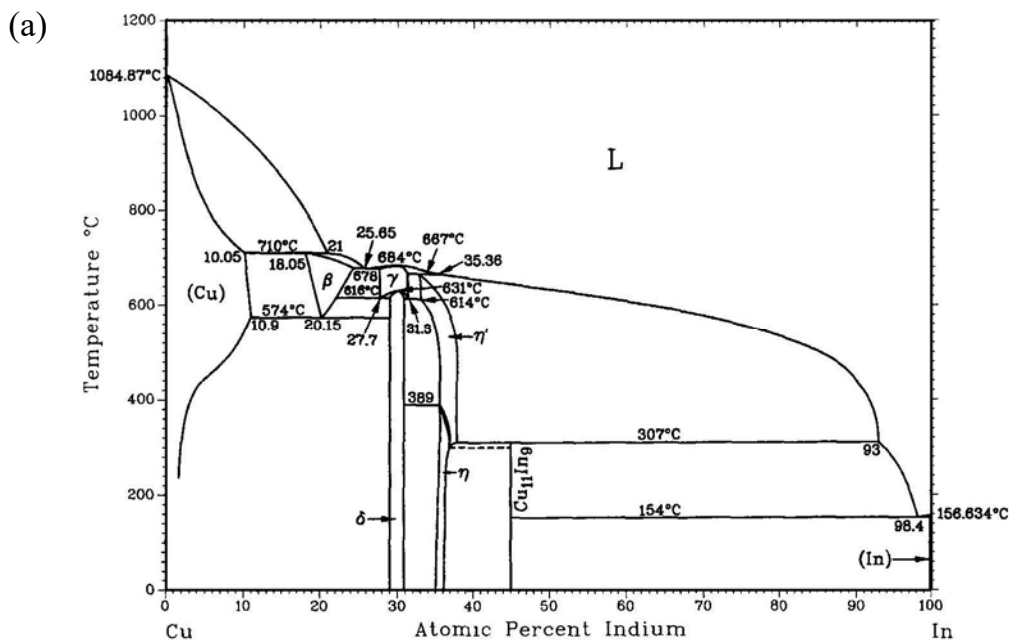
263 We can now summarize the structure evolution of Cu-In bimetallic catalyst NPs (1 nm In/1 nm
264 Cu, nominally 69.6 at.% Cu) throughout the process (Figure 5). During thermal evaporation, Cu is
265 firstly evaporated on the substrate and then In is evaporated on top of Cu. According to the Cu-In
266 binary phase diagram [17, 45-47], Cu_7In_3 (δ) is the stable phase at room temperature under the
267 circumstance of 70 at.% Cu nominal content. However, Cu_7In_3 (δ) phase does not form in the process
268 of thermal evaporation. The deposit obtained upon thermal evaporation has an essentially amorphous
269 structure covered by In native oxide, including only few Cu crystals (Figures 1a and 5). That structure
270 remains so when the 200°C anneal is not performed in the hydrogen plasma. The crystallization of
271 Cu_4In detected after plasma treatment (Figure 1b-d) is thus promoted by the plasma, not the
272 temperature. In the core-shell structure appearing after this treatment, one can evaluate the atomic ratio
273 in the particles, from the volume ratio of the shell in Figure 1c. The latter represents about 59% of the
274 total volume of the NP. Taking the atomic densities of Cu_4In (ICSD file #109480) and of crystalline In
275 (ICSD file #639814), one finds that the In atoms in the shell represent 43% of all the atoms. Adding
276 the In atoms present in the core leads to 54% In, which value represents a maximum, as amorphous In
277 is probably less dense than crystalline In. Overall, such an evaluation appears compatible with the
278 nominal 30% in the deposit, as the latter is subject to the large errors mentioned earlier.

279 When the amorphous Cu-In NPs are processed with the two-step plasma conditions during
280 SiNW growth in the PECVD reactor, we could now summarize the different phase changes as follows
281 (see Figure 5):

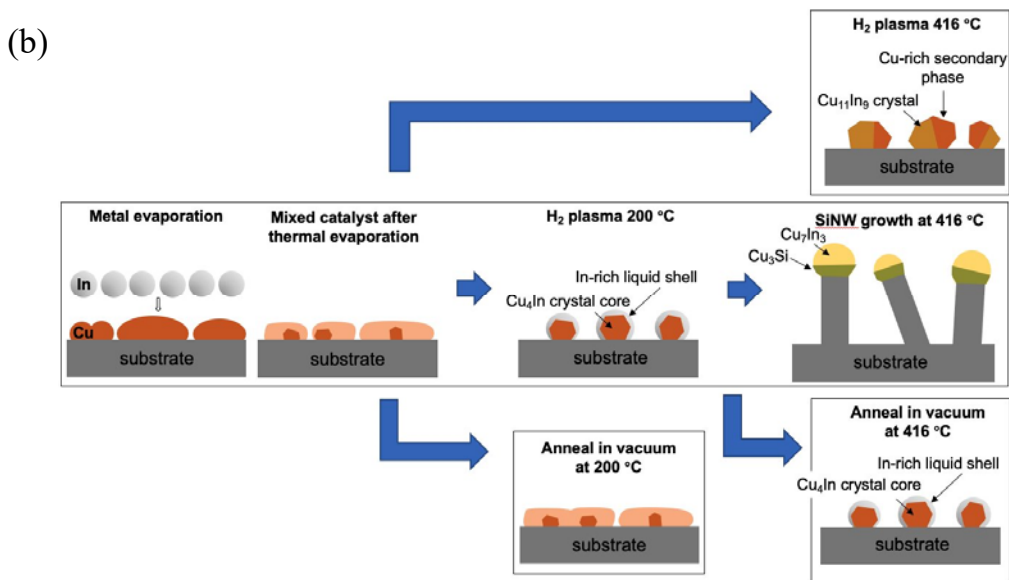
282 I. During the hydrogen plasma pre-treatment at 200 °C (group 1), Cu thus crystallizes under
283 the effect of hydrogen plasma. Let us start by observing that, at this temperature, the In oxide which
284 must be present at the NP surfaces is reduced by the H_2 plasma. The H-plasma induced reduction of In
285 oxide is well known indeed in ITO (indium-tin oxide) [51]. Considering that 200 °C is higher than the
286 melting point of pure indium (156.63 °C), the reduced In melts during this step and forms a liquid

287 layer outside the Cu₄In crystal core (it would stay amorphous upon cooling, hence its structure in the
 288 present TEM observations). If we assume that the surface energy of Cu₄In remains close to that of pure
 289 Cu, we may consider that the surface energy of the NP core stays above 1 Jm⁻² [52], during the whole
 290 H₂-plasma treatment at 200 °C, while that of In remains neatly lower, around 0.5 Jm⁻² [52]. During the
 291 treatment, the liquid indium thus makes a continuous shell around the Cu-based cores, without leaving
 292 the core surfaces exposed to the plasma. However, the phase transition to crystalline Cu₄In, which
 293 does not take place at 200 °C when the plasma is off, remains surprising. We tend to think that the H
 294 atoms provide two things: *i*) they reduce the native In oxide and *ii*) help braking the bonds between
 295 disordered metal atoms; both of these facts lead to an enhanced atomic mobility that corresponds to a
 296 lowering of the potential barriers between the different phases. Moreover, the equilibrium structure in
 297 a NP depends on its surface energy, which, here, is determined by the In coverage. We would propose
 298 that the high-temperature Cu₄Si phase (the β-phase in the phase diagram, Figure 5a) would be
 299 stabilised by this specific particle surface and the fact that In atoms can easily escape liquid In, thanks
 300 to the presence of atomic hydrogen, which helps them to enter the Cu structure.

301



302



303

304 **Figure 5.** (a) Cu-In phase diagram [17], by courtesy of Journal of Phase Equilibria, copyright
 305 Springer Nature. (b) Summary of the evolution of the catalyst NPs after the different treatments. In is
 306 oxidized by air after deposition. Both In and the oxide are amorphous at this stage. The crystalline
 307 cores are very limited in extent, so that a part of the copper can also be amorphous. The 200°C
 308 annealing in H₂ plasma reduces the oxide and helps the cores to form larger crystals, in contrast to the
 309 same annealing without plasma. The SiNW growth conditions – 420°C (group 3), hydrogen-silane
 310 plasma – generate phases different from those obtained with the same annealing but without silane in
 311 the plasma, different themselves from those obtained with same annealing in vacuum.

312 II. By performing the hydrogen plasma treatment on the Cu-In NPs at 420 °C (group 5), the
 313 intermetallic phase Cu₁₁In₉ is obtained (Figure 5). Since Cu₁₁In₉ does not exist above 310 °C according
 314 to the phase diagram [17], we infer that it has formed during cooling. In the control experiment we
 315 carried out at 420°C in vacuum (i.e. without plasma), only very little intermetallic compound is
 316 formed and Cu₄In is essentially preserved. Thus, H atoms generated in the plasma diffuse through the
 317 liquid In and help destabilizing the metastable Cu₄In (let us recall that Cu₄In is stable only above
 318 ~575 °C); In is then able to penetrate the new intermetallic compound, which, following the phase
 319 diagram [46], would be a mixture of In and Cu₇In₃ (δ). Cu₁₁In₉ precipitates when cooled down. Since

320 the nominal Cu at.% is 69.6%, there are residual copper atoms and they exist in the form of Cu
321 crystals as shown in Figure 4b. Thus hydrogen plasma at 420 °C plays an important role for the
322 synthesis of Cu₁₁In₉.

323 Why, now, is it the intermetallic phase Cu₇In₃ (δ) – and not Cu₁₁In₉ – that remains after
324 cooling, when SiH₄ is introduced in the 420°C step? In this case, the *in situ* TEM experiment shows
325 that the SiNW growth follows, at least partially, a VSS mechanism (Figure 3). However, if the
326 mechanism is similar to that observed with Cu-Sn catalysts [13, 15], the solid phase would be
327 essentially made of Cu₃Si, which is detected after cooling (Figure 2) and is compatible with a part of
328 the interplanar spacings measured in Figure 3. The presence of Cu₃Si in the samples indicates that a
329 significant amount of In is left aside during growth, maybe in the form of an In-rich Cu-In compound
330 or, most probably, in the form of Cu-saturated liquid In. Given the fact that Cu solubility in liquid In
331 falls from ~ 9% at 420 °C to ~ 0 at 20 °C [17], in such a scenario, a significant amount of copper
332 would be released during cooling, which would provoke the change of the In-rich Cu-In compound
333 into the Cu-rich Cu₇In₃ (δ) phase. Besides, Cu₃Si remains present indeed, as it is stable at room
334 temperature. In contrast, when no Cu₃Si is present, as in the plasma-treated sample without silane, the
335 copper probably stays in its own phase at 420 °C, at equilibrium with an In-rich Cu-In compound. In
336 this case, there would be no copper atom available to enrich the Cu-In compound during cooling; the
337 latter would, in turn, precipitate in the form of the Cu₁₁In₉ phase, poorer in Cu.

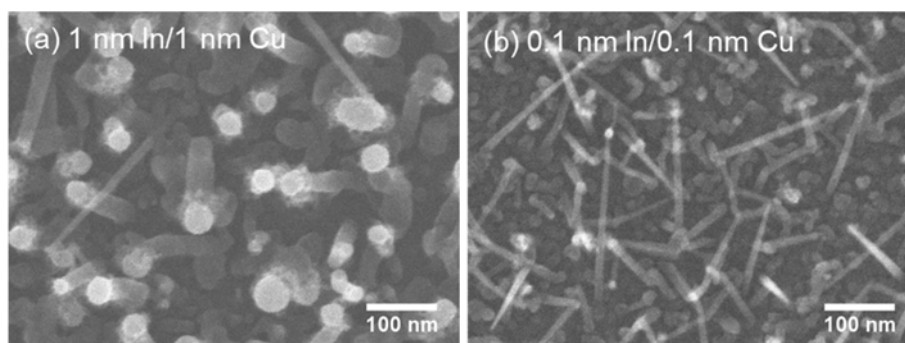
338 In this study, plasma treatment has been proved as an efficient method to induce
339 crystallization, and reaction for the synthesis of the intermetallic phases of copper and indium in the
340 catalyst NPs. Compared with heating, the introduction of atomic hydrogen provides more energy to
341 facilitate the transition of the Cu-In NPs from disorder to order. The H₂-plasma treatment at only
342 200 °C delivers the Cu₄In- β phase normally stable above 574 °C. In addition, in the case of diffusion
343 soldering using pure Cu and pure In solders, it takes 16 days for the formation of Cu₁₁In₉ at 290 °C;
344 and it takes 1.5 hours to synthesize Cu₇In₃ at 430 °C [35]. The reaction rate of Cu₇In₃ in the present
345 case is 30 times faster at a lower temperature (420 °C). By controlling the specific plasma conditions

346 in the PECVD reactor, we manage to control the reactions of the catalyst elements, obtaining various
347 reaction products with a much faster reaction rate. This opens a new way of synthesizing novel alloy
348 catalyst NPs and controlling SiNW growth by using a simple, convenient, fast, and low-cost method
349 combining thermal evaporation and PECVD, which can realize both phase transformation of catalyst
350 NPs and NW growth in the same run of PECVD process.

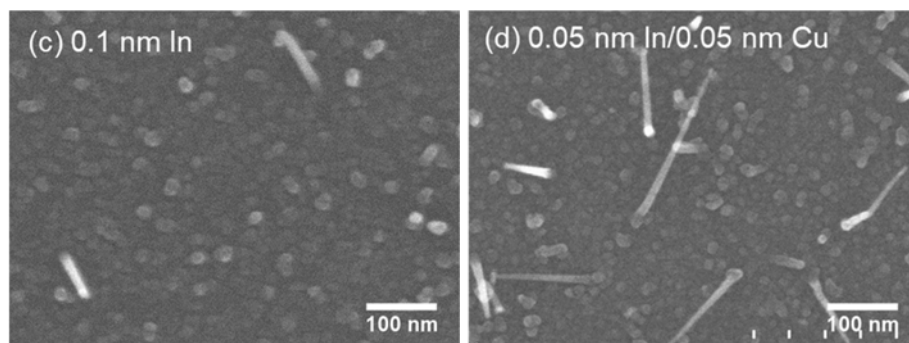
351

352 **3.2. Influence of catalyst composition on the distribution and structure of SiNWs**

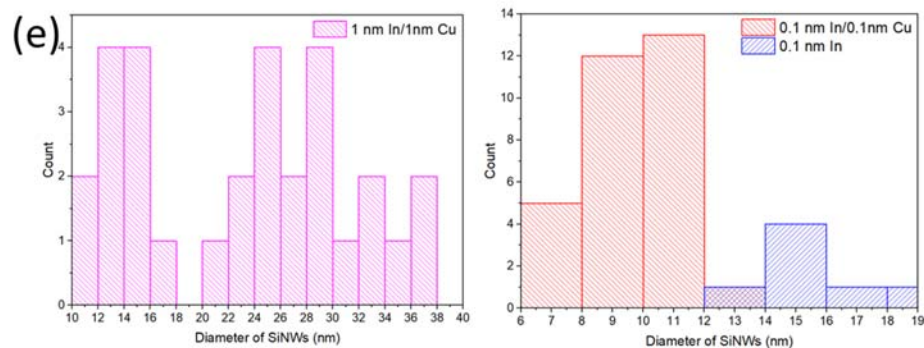
353 In the following section, we focus on the characterization of the morphology, distribution and
354 crystalline structure of the SiNWs fabricated with Cu-In bimetallic catalyst NPs, as a function of
355 catalyst composition, by SEM and TEM. When the SiNWs are synthesized with the 1 nm In/1 nm Cu
356 composition studied above (group 7 to 10), the NW diameter shows a broad distribution: from about
357 10 nm to 38 nm (Figure 6a and e). By decreasing the catalyst nominal thickness to 0.1 nm In/0.1 nm
358 Cu (Figure 6b), the NW diameters have a narrow distribution and are mostly below 12 nm (Figure 6e).
359 The longest NWs have lengths around 300 nm. Meanwhile in the control group where pure In catalyst
360 is used with a nominal thickness of 0.1 nm, the SiNWs obtained are shorter, thicker and much less
361 dense (Figure 6c and e). Previous experience indicates that SiNWs do not grow with pure Cu catalyst
362 under the current conditions [15]. Using Cu-In bimetallic catalysts allows one to adjust the SiNW
363 density, diameter distribution, and growth rate in a range which cannot be realized by using pure
364 metal. Further decreasing the catalyst nominal thickness to 0.05 nm In/0.05 nm only reduces the NW
365 density, while the average diameter (10.5 nm) remains similar (Figure 6d).



366



367

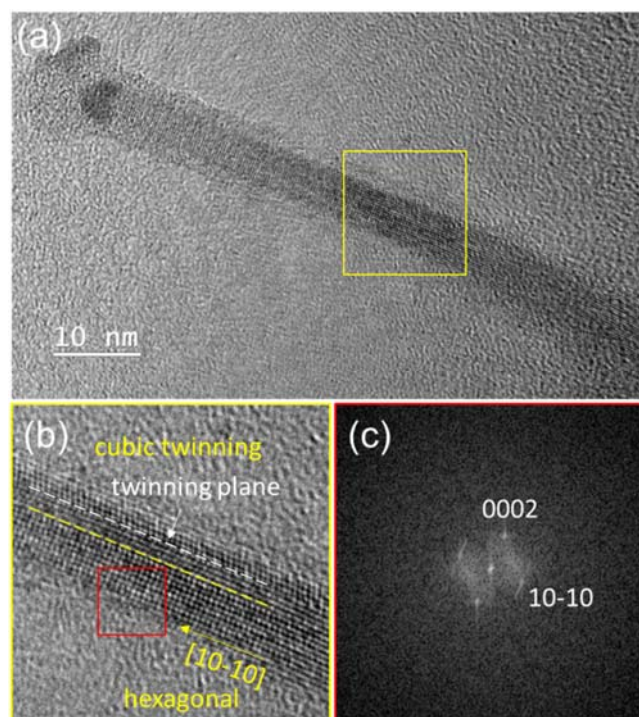


368

369 Figure 6. SEM images of SiNWs grown with (group 7 to 10) mixed catalysts of (a) 1 nm In/1 nm Cu,
 370 (b) 0.1 nm In/0.1 nm Cu, (c) 0.1 nm In, (d) 0.05 nm In/0.05 nm Cu on (100) Si substrates and (e)
 371 histograms of distribution of SiNW diameters.

372 Regarding the structure of the SiNWs themselves, we have searched for the metastable
 373 hexagonal 2H polytype of Si [16], particularly in the sets where the NWs were the narrowest [15]. For
 374 this, we observed more than 50 SiNWs, grown with 0.1 nm In/0.1 nm Cu, by TEM. Among these, 11
 375 SiNWs were in the $[110]_c/[1-210]_H$ zone axis, which is the only zone axis allowing to distinguish the
 376 diamond hexagonal Si phase from the standard diamond cubic Si [39]. Ten of them had cubic
 377 structures, while one of them contained hexagonal phase. The SiNW with hexagonal structure (Figure
 378 7a) has a crystalline core diameter around 5 nm, and a total diameter of 7.5 nm which includes an
 379 amorphous shell. We found there is a catalyst separation phenomenon in this SiNW: in addition to the
 380 catalyst NP connecting to the SiNW crystalline core, there's still an amorphous part above it, on top of
 381 which lies another nanoparticle. Catalyst separation exists not only in the hexagonal NW in Figure 7,
 382 but also in the cubic SiNWs synthesized with the mixed catalyst of 0.1 nm In/0.1 nm Cu. Based on our

383 experience on thin SiNWs catalysed by Cu-Sn co-catalysts [53], we assume that a similar catalyst
384 separation phenomenon has happened after SiNW growth, in the air ambient due to the use of Cu as a
385 catalyst component. An HRTEM image with higher magnification of the selected area in Figure 7a is
386 shown in Figure 7b. The crystalline structure consists of two parts: above the yellow dashed line
387 (which is parallel to the SiNW growth direction) there is a cubic twin with the twin plane indicated by
388 the white dashed line. Below the yellow dashed line, there is a hexagonal phase, which has been
389 confirmed by the FFT pattern shown in Figure 7c, with $d_{(0002)} = 0.314$ nm and $d_{(10-10)} =$
390 0.336 nm. The co-existence of cubic twinning and hexagonal Si does extend to the top of the
391 crystalline core. This configuration, of the 2H structure in a SiNW with a $[211]_C/[11-10]_H$ growth axis,
392 was quite rare in our previous observations of that phase in Cu-Sn catalysed SiNWs [15, 39], where
393 the dominant configuration was with a $[0001]$ growth axis, and where the present geometry only
394 occurred after a right-angle change of growth direction [39]. Thus, the mechanism of formation of that
395 metastable phase would be original in the present case, perhaps involving the atomic structure of the
396 $\text{Cu}_7\text{In}_3/\text{Si}$ interface at start of the VSS growth.



398 Figure 7. (a) HRTEM image of a SiNW synthesized with 0.1 nm In/0.1 nm Cu co-catalyst,
399 transferred on a carbon-coated gold TEM grid from (100) Si substrate; (b) enlarged view of the
400 yellow-squared area in (a), showing the co-existence of cubic twinning and hexagonal Si along the
401 NW growth direction; (c) FFT image of the red-squared area in (b) showing a pattern of hexagonal Si.

402 In addition, we have also characterized by TEM the crystalline structures of thicker SiNWs
403 synthesized with a mixed catalyst of 1 nm In/1 nm Cu (Figure 6a and d). All of the observed SiNWs
404 had diameters larger than 15 nm and all of them showed cubic phase.

405 4. Conclusions

406 We have studied the structure evolution of thermally-evaporated Cu-In bimetallic NPs
407 throughout the SiNW growth process, with *in-situ* as well as *ex-situ* TEM observations. The *ex-situ*
408 process includes a hydrogen plasma pre-treatment in the PECVD reactor at a temperature of 200 °C
409 and the growth process itself, in a H₂-SiH₄ plasma, in the same reactor at 420 °C. We show that the
410 200°C pre-treatment induces a partial crystallization of the essentially amorphous as-deposited NPs,
411 leading to a structure including a crystalline core (Cu₄In)-β and a liquid shell (In); we also show that
412 applying the hydrogen plasma treatment at SiNW growth temperature (420 °C), but without SiH₄,
413 induces the formation of the intermetallic phase Cu₁₁In₉ in the NPs. Quite interestingly, adding silane
414 to the plasma changes that phase found after growth to Cu₇In₃ (δ). The *in situ* experiments show that
415 the SiNWs synthesized with Cu-In bimetallic catalyst NPs with the hydrogen-silane plasma follow an
416 essentially “VSS” PECVD process but does not rule out the presence of liquid part in the catalyst. By
417 adjusting the composition of the bimetallic Cu-In catalyst NPs, we have obtained dense SiNW arrays
418 with a smallest average diameter around 10 nm and a narrow distribution that we could never realize
419 with pure metal catalysts. Moreover, we were able to fabricate a SiNW (crystalline diameter of 5 nm)
420 that includes a large hexagonal domain (which is predicted to have a direct bandgap). We believe that
421 further studies on compound catalysts in general, and especially liquid-solid ones, could lead to a fine
422 control not only of SiNW shape and density, but ultimately of their crystalline phase, opening up new

423 prospects for crystal-phase heterostructures at the nanoscale.

424 **References**

425

426

427

- 428 1. Hu, J.; Odom, T. W.; Lieber, C. M., Chemistry and physics in one dimension: Synthesis and
429 properties of nanowires and nanotubes. *Acc. Chem. Res.* **1999**, *32*, 435-445. doi:
430 10.1021/ar9700365
- 431 2. Lieber, C. M.; Wang, Z. L., Functional Nanowires. *MRS Bull.* **2011**, *32*, 99-108. doi:
432 10.1557/mrs2007.41
- 433 3. Zhang, A.; Zheng, G.; Lieber, C. M., Emergence of Nanowires. In *Nanowires: Building*
434 *Blocks for Nanoscience and Nanotechnology*, Zhang, A.; Zheng, G.; M. Lieber, C., Eds.
435 Springer International Publishing: Cham, 2016; pp 1-13.
- 436 4. Lysov, A.; Vinaji, S.; Offer, M.; Gutsche, C.; Regolin, I.; Mertin, W.; Geller, M.; Prost, W.;
437 Bacher, G.; Tegude, F.-J., Spatially resolved photoelectric performance of axial GaAs
438 nanowire pn-diodes. *Nano Research* **2011**, *4*, 987-995. doi: 10.1007/s12274-011-0155-4
- 439 5. Chen, K.-I.; Li, B.-R.; Chen, Y.-T., Silicon nanowire field-effect transistor-based biosensors
440 for biomedical diagnosis and cellular recording investigation. *Nano Today* **2011**, *6*, 131-154.
441 doi: 10.1016/j.nantod.2011.02.001
- 442 6. Könenkamp, R.; Word, R. C.; Schlegel, C., Vertical nanowire light-emitting diode. *Appl.*
443 *Phys. Lett.* **2004**, *85*, 6004-6006. doi: 10.1063/1.1836873
- 444 7. Tong, C.; Delamarre, A.; De Lépinau, R.; Scaccabarozzi, A.; Oehler, F.; Harmand, J.-C.;
445 Collin, S.; Cattoni, A., GaAs/GaInP nanowire solar cell on Si with state-of-the-art Voc and
446 quasi-Fermi level splitting. *Nanoscale* **2022**, *14*, 12722-12735. doi: 10.1039/D2NR02652J
- 447 8. Wagner, R. S.; Ellis, W. C., Vapor-liquid-solid mechanism of single crystal growth. *Appl.*
448 *Phys. Lett.* **1964**, *4*, 89-90. doi: 10.1063/1.1753975
- 449 9. Cui, Y.; Lieber, C. M., Functional nanoscale electronic devices assembled using silicon
450 nanowire building blocks. *Science* **2001**, *291*, 851-3. doi: 10.1126/science.291.5505.851
- 451 10. Puglisi, R. A.; Bongiorno, C.; Caccamo, S.; Fazio, E.; Mannino, G.; Neri, F.; Scalse, S.;
452 Spucches, D.; La Magna, A., Chemical Vapor Deposition Growth of Silicon Nanowires with
453 Diameter Smaller Than 5 nm. *ACS Omega* **2019**, *4*, 17967-17971. doi:
454 10.1021/acsomega.9b01488
- 455 11. Holmes, J. D.; Johnston, K. P.; Doty, R. C.; Korgel, B. A., Control of thickness and
456 orientation of solution-grown silicon nanowires. *Science* **2000**, *287*, 1471-3. doi:
457 10.1126/science.287.5457.1471
- 458 12. Kuykendall, T. R.; Altoe, M. V. P.; Ogletree, D. F.; Aloni, S., Catalyst-directed
459 crystallographic orientation control of GaN nanowire growth. *Nano Lett.* **2014**, *14*, 6767-6773.
460 doi: 10.1021/nl502079v
- 461 13. Ngo, É.; Wang, W.; Bulkin, P.; Florea, I.; Foldyna, M.; Roca i Cabarrocas, P.; Maurice, J.-L.,
462 Liquid-assisted vapor–solid–solid silicon nanowire growth mechanism revealed by in situ
463 TEM when using Cu–Sn bimetallic catalysts. *J. Phys. Chem. C* **2021**, *125*, 19773-19779. doi:
464 10.1021/acs.jpcc.1c05402
- 465 14. Hu, T.; Seifner, M. S.; Snellman, M.; Jacobsson, D.; Sedrpooshan, M.; Ternero, P.; Messing,
466 M. E.; Dick, K. A., Direct observation of liquid–solid two-phase seed particle-assisted kinking
467 in GaP nanowire growth. *Small Structures* **2023**, *n/a*, 2300011. doi: 10.1002/sstr.202300011

- 468 15. Wang, W.; Ngo, É.; Florea, I.; Foldyna, M.; Roca i Cabarrocas, P.; Maurice, J.-L., High
469 density of quantum-sized silicon nanowires with different polytypes grown with bimetallic
470 catalysts. *ACS Omega* **2021**, *6*, 26381-26390. doi: 10.1021/acsomega.1c03630
- 471 16. Amato, M.; Kaewmaraya, T.; Zobelli, A.; Palummo, M.; Rurali, R., Crystal phase effects in Si
472 nanowire polytypes and their homojunctions. *Nano Lett* **2016**, *16*, 5694-700. doi:
473 10.1021/acs.nanolett.6b02362
- 474 17. Okamoto, H., Comment on Cu-In (Copper-Indium). *J. Phase Equilib.* **1994**, *15*, 226-227. doi:
475 10.1007/BF02646373
- 476 18. Olesinski, R.; Kanani, N.; Abbaschian, G., The In Si (Indium-Silicon) system. *Bulletin of*
477 *Alloy Phase Diagrams* **1985**, *6*, 128-130. doi:
- 478 19. Yu, L.; Chen, W.; O'Donnell, B.; Patriarche, G.; Bouchoule, S.; Pareige, P.; Rogel, R.; Claire
479 Salaun, A.; Pichon, L.; Roca i Cabarrocas, P., Growth-in-place deployment of in-plane silicon
480 nanowires. *Appl. Phys. Lett.* **2011**, *99*. doi: 10.1063/1.3659895
- 481 20. Kim, D.-G.; Lee, C.-Y.; Jung, S.-B., Interfacial reactions and intermetallic compound growth
482 between indium and copper. *J. Mater. Sci.: Mater. Electron.* **2004**, *15*, 95-98. doi:
483 10.1023/B:JMSE.0000005383.95823.13
- 484 21. Orbey, N.; Birkmire, R. W.; Russell, T. W. F.; Jones, G. A., Copper-Indium Alloy
485 Transformations. *J. Phase Equilib.* **2000**, *21*, 509. doi: 10.1007/s11669-000-0018-2
- 486 22. Park, J.-S.; Jeong, J. K.; Chung, H.-J.; Mo, Y.-G.; Kim, H. D., Electronic transport properties
487 of amorphous indium-gallium-zinc oxide semiconductor upon exposure to water. *Appl. Phys.*
488 *Lett.* **2008**, *92*, 072104. doi: 10.1063/1.2838380
- 489 23. Ramanujam, J.; Singh, U. P., Copper indium gallium selenide based solar cells – a review.
490 *Energy Environ. Sci.* **2017**, *10*, 1306-1319. doi: 10.1039/C7EE00826K
- 491 24. Scofield, J. H.; Duda, A.; Albin, D.; Ballard, B. L.; Predecki, P. K., Sputtered molybdenum
492 bilayer back contact for copper indium diselenide-based polycrystalline thin-film solar cells.
493 *Thin Solid Films* **1995**, *260*, 26-31. doi: 10.1016/0040-6090(94)06462-8
- 494 25. Yang, J.; Kim, J.-Y.; Yu, J. H.; Ahn, T.-Y.; Lee, H.; Choi, T.-S.; Kim, Y.-W.; Joo, J.; Ko, M.
495 J.; Hyeon, T., Copper–indium–selenide quantum dot-sensitized solar cells. *Phys. Chem. Chem.*
496 *Phys.* **2013**, *15*, 20517-20525. doi: 10.1039/C3CP54270J
- 497 26. Yu, C. L.; Wang, S. S.; Chuang, T. H., Intermetallic compounds formed at the interface
498 between liquid indium and copper substrates. *J. Electron. Mater.* **2002**, *31*, 488-493. doi:
499 10.1007/s11664-002-0104-9
- 500 27. Castilla-Amorós, L.; Schouwink, P.; Oveisi, E.; Okatenko, V.; Buonsanti, R., Tailoring
501 morphology and elemental distribution of Cu-In nanocrystals via galvanic replacement. *J. Am.*
502 *Chem. Soc.* **2022**, *144*, 18286-18295. doi: 10.1021/jacs.2c05792
- 503 28. Rasul, S.; Anjum, D. H.; Jedidi, A.; Minenkov, Y.; Cavallo, L.; Takanabe, K., A Highly
504 Selective Copper–Indium Bimetallic Electrocatalyst for the Electrochemical Reduction of
505 Aqueous CO₂ to CO. *Angew. Chem. Int. Ed.* **2015**, *54*, 2146-2150. doi:
506 10.1002/anie.201410233
- 507 29. Luo, W.; Xie, W.; Mutschler, R.; Oveisi, E.; De Gregorio, G. L.; Buonsanti, R.; Züttel, A.,
508 Selective and Stable Electroreduction of CO₂ to CO at the Copper/Indium Interface. *ACS*
509 *Catalysis* **2018**, *8*, 6571-6581. doi: 10.1021/acscatal.7b04457
- 510 30. Ahn, S.; Choi, Y. J.; Kim, K.; Eo, Y.-J.; Cho, A.; Gwak, J.; Yun, J. H.; Shin, K.; Ahn, S. K.;
511 Yoon, K., Amorphous Cu–In–S Nanoparticles as Precursors for CuInSe₂ Thin-Film Solar
512 Cells with a High Efficiency. *ChemSusChem* **2013**, *6*, 1282-1287. doi:
513 10.1002/cssc.201200894
- 514 31. Ahn, S.; Kim, C.; Yun, J. H.; Gwak, J.; Jeong, S.; Ryu, B.-H.; Yoon, K., CuInSe₂ (CIS) Thin
515 Film Solar Cells by Direct Coating and Selenization of Solution Precursors. *J. Phys. Chem. C*
516 **2010**, *114*, 8108-8113. doi: 10.1021/jp1007363
- 517 32. Stolt, L.; Hedström, J.; Kessler, J.; Ruckh, M.; Velthaus, K. O.; Schock, H. W.,
518 ZnO/CdS/CuInSe₂ thin-film solar cells with improved performance. *Appl. Phys. Lett.* **1993**,
519 *62*, 597-599. doi: 10.1063/1.108867

- 520 33. Sommadossi, S.; Gust, W.; Mittemeijer, E. J., Phase characterisation and kinetic behaviour of
521 diffusion soldered Cu/In/Cu interconnections. *Mater. Sci. Technol.* **2003**, *19*, 528-534. doi:
522 10.1179/026708303225009706
- 523 34. Sommadossi, S.; Litynska, L.; Zieba, P.; Gust, W.; Mittemeijer, E. J., Transmission electron
524 microscopy investigation of the microstructure and chemistry of Si/Cu/In/Cu/Si
525 interconnections. *Mater. Chem. Phys.* **2003**, *81*, 566-568. doi: 10.1016/S0254-0584(03)00076-
526 2
- 527 35. Wojewoda, J.; Zieba, P.; Faryna, M.; Gust, W.; Mittemeijer, E. J.; Litynska, L.,
528 Characterization of Interfacial Reactions in Cu/In/Cu Joints. *Microchimica Acta* **2004**, *145*,
529 107-110. doi: 10.1007/s00604-003-0138-6
- 530 36. Wang, W. Plasma-enhanced CVD growth of cubic and hexagonal diamond silicon nanowires
531 with liquid-solid mixed catalysts for photovoltaic applications. PhD Thesis, Institut
532 Polytechnique de Paris, 2021.
- 533 37. Maurice, J.-L.; Bulkin, P.; Ngo, É.; Wang, W.; Foldyna, M.; Florea, I.; Roca i Cabarrocas, P.;
534 Béjaud, R.; Hardouin Duparc, O., Visualizing the effects of plasma-generated H atoms in situ
535 in a transmission electron microscope. *Eur. Phys. J. Appl. Phys.* **2022**, *97*. doi:
536 10.1051/epjap/2022210276
- 537 38. Liu, X.; Davis, R. W.; Hughes, L. C.; Rasmussen, M. H.; Bhat, R.; Zah, C.-E.; Stradling, J., A
538 study on the reliability of indium solder die bonding of high power semiconductor lasers. *J.*
539 *Appl. Phys.* **2006**, *100*, 013104. doi: 10.1063/1.2209194
- 540 39. Tang, J.; Maurice, J. L.; Fossard, F.; Florea, I.; Chen, W.; Johnson, E. V.; Foldyna, M.; Yu,
541 L.; Roca, I. C. P., Natural occurrence of the diamond hexagonal structure in silicon nanowires
542 grown by a plasma-assisted vapour-liquid-solid method. *Nanoscale* **2017**, *9*, 8113-8118. doi:
543 10.1039/c7nr01299c
- 544 40. Stadelmann, P. A., EMS - a software package for electron diffraction analysis and HREM
545 image simulation in materials science. *Ultramicroscopy* **1987**, *21*, 131-145. doi:
546 10.1016/0304-3991(87)90080-5
- 547 41. Stadelmann, P. JEMS-Swiss. <https://www.jems-swiss.ch/>
- 548 42. Zoubian, F.; Renaut, N.; Latrassé, L., Distributed elementary ECR microwave plasma sources
549 supplied by solid state generators for production of large area plasmas without scale
550 limitation: plasma density measurements and comparison with simulation. *Plasma Research*
551 *Express* **2021**, *3*, 025010. doi: 10.1088/2516-1067/ac0499
- 552 43. Sigeneger, F.; Ellis, J.; Harhausen, J.; Lang, N.; van Helden, J. H., Verified modeling of a low
553 pressure hydrogen plasma generated by electron cyclotron resonance. *Plasma Sources Sci.*
554 *Technol.* **2022**, *31*, 105011. doi: 10.1088/1361-6595/ac963e
- 555 44. Che, G. C.; Ellner, M., Powder crystal data for the high-temperature phases Cu₄In, Cu₉In₄(h)
556 and Cu₂In(h). *Powder Diffr.* **2013**, *7*, 107-108. doi: 10.1017/s0885715600018340
- 557 45. Bolcavage, A.; Chen, S. W.; Kao, C. R.; Chang, Y. A.; Romig, A. D., Phase equilibria of the
558 Cu-In system I: Experimental investigation. *J. Phase Equilib.* **1993**, *14*, 14-21. doi:
559 10.1007/BF02652157
- 560 46. Subramanian, P. R.; Laughlin, D. E., The Cu–In (Copper-Indium) system. *Bulletin of Alloy*
561 *Phase Diagrams* **1989**, *10*, 554-568. doi: 10.1007/bf02882415
- 562 47. Bahari, Z.; Dichi, E.; Legendre, B.; Dugué, J., The equilibrium phase diagram of the copper–
563 indium system: a new investigation. *Thermochim. Acta* **2003**, *401*, 131-138. doi:
564 10.1016/s0040-6031(02)00500-2
- 565 48. Koster, A. S.; Wolff, L. R.; Visser, G. J., Structure of copper–indium Cu₇In₃. *Acta*
566 *Crystallogr. B Struct. Crystallogr. Cryst. Chem.* **1980**, *36*, 3094-3096. doi:
567 10.1107/s0567740880010886
- 568 49. Yao, Y.; Fan, S., Si nanowires synthesized with Cu catalyst. *Mater. Lett.* **2007**, *61*, 177-181.
569 doi: 10.1016/j.matlet.2006.04.045
- 570 50. Rajasekharan, T. P.; Schubert, K., Kristallstruktur von Cu₁₁In₉. *International Journal of*
571 *Materials Research* **1981**, *72*, 275-278. doi: doi:10.1515/ijmr-1981-720410

- 572 51. Drevillon, B.; Kumar, S.; Roca i Cabarrocas, P.; Siefert, J., In situ investigation of the
573 optoelectronic properties of transparent conducting oxide/amorphous silicon interfaces. *Appl.*
574 *Phys. Lett.* **1989**, *54*, 2088-2090. doi:
575 52. Campbell, C. T., Ultrathin metal films and particles on oxide surfaces: structural, electronic
576 and chemisorptive properties. *Surf. Sci. Rep.* **1997**, *27*, 1-111. doi: 10.1016/S0167-
577 5729(96)00011-8
578 53. Wang, W.; Ngo, É.; Florea, I.; Foldyna, M.; Roca i Cabarrocas, P.; Maurice, J.-L., Room
579 temperature growth of silica nanowires on top of ultrathin Si nanowires synthesized with Sn-
580 Cu bimetallic seeds. *Phys. Status Solidi A* **2021**, *218*, 2100409. doi: 10.1002/pssa.202100409
581